



# Probing ultraweak in-plane magnetic anisotropy within a two-dimensional layered antiferromagnet

Yijie Fan<sup>a,b</sup> , Yihong Xu<sup>a,b</sup> , Renji Bian<sup>c</sup>, Ruan Zhang<sup>a,b</sup>, Junning Mei<sup>a,b</sup>, Jiaxin Wu<sup>a,b</sup>, Binghe Xie<sup>a,b</sup>, Shuangxing Zhu<sup>a,b</sup>, Yu Chen<sup>a,b</sup>, Feifan Gu<sup>a,b</sup>, Ying Liu<sup>a,b</sup>, Takashi Taniguchi<sup>d</sup>, Kenji Watanabe<sup>d</sup> , Fucui Liu<sup>c,e,f</sup>, and Xinghan Cai<sup>a,1</sup>

Affiliations are included on p. 6.

Edited by Liuyan Zhao, University of Michigan, Ann Arbor, MI; received July 21, 2024; accepted February 18, 2025 by Editorial Board Member Risto Nieminen

Magnetic anisotropy plays a crucial role in determining the critical behavior and phase transitions in two-dimensional magnetic systems. It is also required for the design of thin-film spintronic devices. Despite its significance, sensing extremely weak anisotropy has proven challenging in van der Waals antiferromagnetic/ferrimagnetic materials. Here, we first employ simulations of micromagnetic energy function in few-layer easy-plane antiferromagnetic systems with a weak additional uniaxial anisotropy and unveil an intriguing even-odd effect closely linked to low-field spin-flip behaviors. We further perform tunneling magneto-conductance measurements on a model 2D antiferromagnetic insulator,  $\text{CrCl}_3$ , exhibiting near-ideal easy-plane anisotropy. The magnetic field-controlled tunneling current at low temperature aligns well with simulated in-plane anisotropic spin-configuration, providing direct experimental evidence for detecting magnetic anisotropy field around 1 mT. Our work creates opportunities for finely characterizing magnetic structures and behaviors in 2D antiferromagnetic/ferrimagnetic systems, with potential applications in spintronics such as data storage and magnetic sensing.

magnetic anisotropy | magnetic tunnel junction | 2D material |  $\text{CrCl}_3$

Magnetic anisotropy refers to the preferred direction of magnetization in a material, which arises from various factors, such as the atomic structure of the crystal, the demagnetizing field induced by its shape, and the magnetic exchange coupling (1–4). Understanding magnetic systems, particularly the recently discovered two-dimensional (2D) van der Waals magnetic materials, necessitates consideration of this significant factor. For instance, the presence of Ising-type out-of-plane anisotropy in  $\text{CrI}_3$  and  $\text{Fe}_3\text{GeTe}_2$  stabilizes the long-range 2D magnetic order, effectively circumventing the constraints imposed by the Mermin–Wagner theorem (5, 6). The monolayer  $\text{CrCl}_3$ , an almost perfect easy-plane magnetic system, demonstrates a finite-size Berezinskii–Kosterlitz–Thouless phase transition (7). Additionally, the magnetic anisotropy in van der Waals magnet is indispensable in designing spintronic devices. It is imperative for magnetic hysteresis, ensuring the existence of the nonvolatile states for magnetic storage. Strong magnetic anisotropy provides adequate coercivity to avoid information confusion and ensures long-term stability (8–10), while weak magnetic anisotropy offers benefits for high switching speed and minimized energy consumption (11–13). Consequently, detecting and tuning magnetic anisotropy hold great importance in 2D magnetic systems (*SI Appendix, Text 11*).

Traditional methods used to investigate the magnetic anisotropy typically involve analyzing the magnetization in bulk materials or large-area epitaxial thin films with an applied magnetic field, such as the superconducting quantum interference device (SQUID) (14, 15), vibrating sample magnetometer (VSM) (16), NMR (17), and broadband ferromagnetic resonance (FMR) (18). However, these methods are not practical for atomically thin exfoliated 2D magnetic materials due to their reduced sizes and resulting low signal-to-noise ratio. In order to characterize micrometer-sized van der Waals magnets, Hall measurements and magneto-optical approaches like magneto-optical Kerr effect (MOKE) and reflective magnetic circular dichroism (RMCD) are commonly used (19–21). Hall measurements are limited to metallic or semiconducting materials, while MOKE or RMCD is effective for detecting out-of-plane magnetization, but struggles with in-plane magnetic components, requiring complex modifications to the experimental setup. Microscopic methods like magnetic force microscopy (MFM) (22–24), scanning SQUID-on-tip (SOT) microscopy (25, 26), scanning tunneling microscopy (STM) (27), and scanning single-spin magnetometry based on single nitrogen-vacancy (NV) center in diamond (28) may be useful for detecting magnetic anisotropy in 2D systems but require further experimental verification. To summarize, probing magnetic anisotropy, particularly ultraweak in-plane

## Significance

Magnetic anisotropy is essential for understanding the critical behavior of 2D magnetic systems and is indispensable in the development of thin-film spintronic devices. However, the investigation of weak, particularly in-plane magnetic anisotropy in van der Waals systems presents significant challenges, yet it holds potential value in scientific research on low-dimensional magnetism and device applications. Here, we propose using a  $\text{CrCl}_3$  magnetic tunnel junction (MTJ) to investigate the in-plane magnetic anisotropy by observing the tunneling current while continuously rotating an in-plane magnetic field. Yielding consistent results between experiment and simulation, our work demonstrates an effective approach for probing weak in-plane magnetic anisotropy at the scale of 1 mT, which can be applied to diverse layered antiferromagnetic or ferrimagnetic systems.

Author contributions: X.C. designed research; Y.F., Y.X., R.B., R.Z., J.M., J.W., B.X., S.Z., Y.C., F.G., Y.L., T.T., K.W., and F.L. performed research; Y.F., F.L., and X.C. analyzed data; and Y.F. and X.C. wrote the paper.

The authors declare no competing interest.

This article is a PNAS Direct Submission. L.Z. is a guest editor invited by the Editorial Board.

Copyright © 2025 the Author(s). Published by PNAS. This article is distributed under Creative Commons Attribution-NonCommercial-NoDerivatives License 4.0 (CC BY-NC-ND).

<sup>1</sup>To whom correspondence may be addressed. Email: xhcai@sjtu.edu.cn.

This article contains supporting information online at <https://www.pnas.org/lookup/suppl/doi:10.1073/pnas.2414668122/-/DCSupplemental>.

Published April 8, 2025.

magnetic anisotropy, in micrometer-sized 2D magnetic insulators can be extremely challenging.

In this study, we propose the fabrication of a magnetic tunnel junction (MTJ) device using a layered antiferromagnetic insulator as the tunnel barrier to investigate its in-plane magnetic anisotropy through tunneling magneto-resistance (TMR) measurements. Here, “in-plane anisotropy” signifies behavior variations of the material in response to magnetic fields in different in-plane directions, deviating from the ideal XY model. The tunneling current, influenced by the spin-filtering effect (8), can be used to monitor the magnetic state with rotating in-plane magnetic field (29). In our simulations, we observe a continuously changing anisotropic TMR in MTJs with even-layer tunnel barriers, whereas MTJs with odd-layer tunnel barriers exhibit an abrupt change in the tunneling current by rotating the in-plane magnetic field, which can be traced back to the low-field spin-flop transition and directly correlates with the magnetic anisotropy. We experimentally confirm the simulated anisotropic TMR in 2D MTJs based on atomically thin  $\text{CrCl}_3$ , a layered antiferromagnet with extremely weak in-plane anisotropy (in-plane anisotropy field  $\sim 10$  Oe for bulk  $\text{CrCl}_3$  crystal) (17, 30–32). Our method is effective in detecting subtle magnetic anisotropy that is not restricted to a specific material. It can be readily extended to other layered antiferromagnetic or ferrimagnetic systems, regardless of their micrometer size and atomic thickness (*SI Appendix, Text 10*).

## Results and Discussion

**Simulation of the Micromagnetic Energy Function.** We start to model the change in the magnetic state of a layered antiferromagnetic insulator (see Fig. 3*A* For illustrations of its magnetic configuration) with almost complete easy-plane (and within the plane, very weak uniaxial) anisotropy as it undergoes continuous in-plane field rotation. To simplify the description of the system, we assume that the magnetic moments remain oriented in the in-plane direction throughout this process, which is a reasonable assumption for easy-plane systems. Consequently, each magnetic moment vector in the material can be effectively represented using the in-plane azimuth angle. When an in-plane magnetic field is applied, the micromagnetic energy of an  $N$ -layer antiferromagnet, taking into account interlayer interaction, Zeeman energy, and in-plane uniaxial anisotropy energy, can be expressed as follows (assuming the magnetic moments are always parallel-aligned within a single layer) (33, 34):

$$\frac{U_N}{\mu_0 M_s} = \frac{1}{2} H_E \sum_{i=1}^{N-1} \cos(\phi_{i+1} - \phi_i) - H \sum_{i=1}^N \cos \phi_i + H_A \sum_{i=1}^N \sin^2(\phi_i + \delta), \quad [1]$$

where  $U_N$  is micromagnetic energy per unit space,  $\mu_0$  is magnetic permeability of vacuum,  $M_s$  is the saturation magnetization of a single layer,  $H_E$ ,  $H$ , and  $H_A$  are the interlayer exchange field, external magnetic field, and uniaxial anisotropy field, respectively,  $\phi_i$  is the angle between the magnetic moment of the  $i$ th layer and in-plane field and  $\delta$  is the angle between the in-plane field and easy axis. In the presence of an external magnetic field, the system will adopt a configuration that minimizes the micromagnetic energy. The calculations are performed on antiferromagnetic systems consisting of two and three layers (See *SI Appendix, Fig. S6* for results related to a four-layer system). In these configurations, Eq. 1 can be simplified as Eq. 2 for two-layer case and Eq. 3 for three-layer case:

$$\frac{U_2}{\mu_0 M_s} = \frac{1}{2} H_E \cos(\theta) - H (\cos(\phi) + \cos(\phi + \theta)) + H_A (\sin^2(\phi + \delta) + \sin^2(\phi + \theta + \delta)), \quad [2]$$

$$\frac{U_3}{\mu_0 M_s} = H_E \cos(\theta) - H (2\cos(\phi) + \cos(\phi + \theta)) + H_A (2\sin^2(\phi + \delta) + \sin^2(\phi + \theta + \delta)), \quad [3]$$

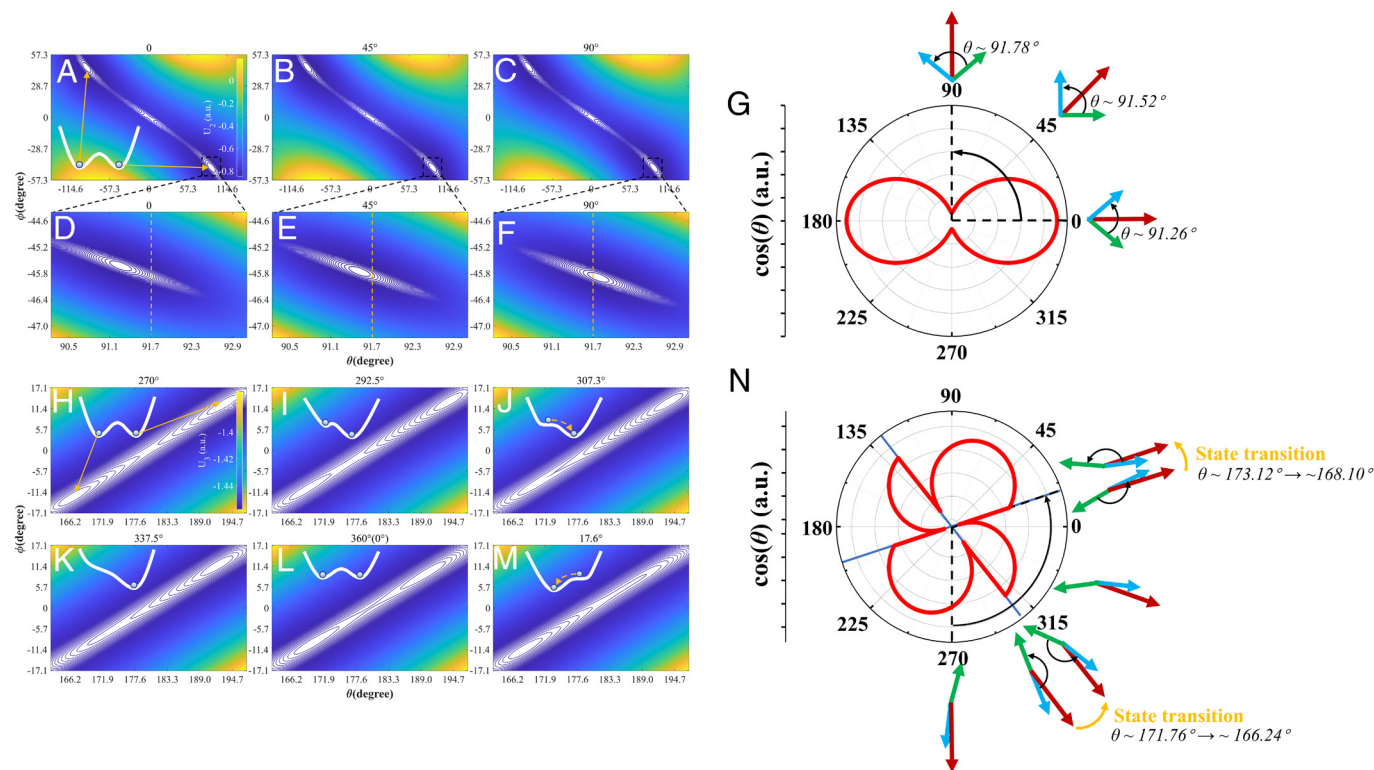
where  $\phi$  denotes the angle between the magnetic moment of the first layer and the magnetic field and  $\theta$  represents the angle between the magnetic moments of adjacent layers (In the trilayer sample, the magnetic moments of the first and third layers are always aligned in the same direction). For the simulations, the anisotropy field  $\mu_0 H_A$  is consistently set to be 1 mT (17, 30, 31). The exchange field  $\mu_0 H_E$  for the bilayer and trilayer samples are set at 0.86 T and 0.96 T, respectively (3); further details can be found in *SI Appendix, Text 1*.

Fig. 1 illustrates contour plots of the micromagnetic energy in the  $\theta - \phi$  phase space, with a magnetic field applied at selected in-plane orientations. The local minimum in the contour plots represents the stable state of the system. For the bilayer case, a moderate magnetic field strength of  $\mu_0 H = 0.6$  T is selected, and the contour plots are presented as the angle  $\delta$  varies from 0 to 90°, representing the magnetic field rotating from parallel to perpendicular with respect to the easy axis. All plots reveal a degenerate bistable state (Fig. 1*A–C*), which persists throughout the entire rotation process. Variations in  $\delta$  result in slight adjustments to the corresponding state variable  $\theta$  (which influences the tunneling conductance, as discussed in the next section; also see *SI Appendix, Text 2*) due to the presence of magnetic anisotropy, as depicted in Fig. 1*D–F*. In Fig. 1*G*, we present the change in  $\cos(\theta)$  as the external magnetic field completes a 360° rotation, revealing a two-fold symmetrical spindle shape.

The evolution of the trilayer micromagnetic energy function in response to an external magnetic field is more complex. Fig. 1*H–M* shows the contour plots of the micromagnetic energy for a trilayer sample as the external field angle rotates approximately 110° while the field strength is maintained at  $\mu_0 H = 0.5$  T (for simulations results at additional field strengths, see *SI Appendix, Text 3 and Fig. S2*). At  $\delta = 270^\circ$ , the function exhibits degenerate bistable states (inset of Fig. 1*H*). As the magnetic field rotates counterclockwise, the energy of one state increases while the barrier on its side diminishes (Fig. 1*I*). As the rotation approaches a critical  $\delta$  near 307.3° (Fig. 1*J*), this state becomes unstable, promoting the system to transition to a single stable state (Fig. 1*K*), where it remains until further changes occur (Fig. 1*L* and *M*). This state transition results in a sudden alternation of the angle ( $\theta$ ) between the magnetic moments in adjacent layers, as indicated by the schematics shown in Fig. 1*N*. In Fig. 1*N*, we plot the variation of  $\cos(\theta)$  relative to a complete counterclockwise rotation of the magnetic field, which yields four jumps corresponding to the magnetic state transitions.

**Simulation of the Tunneling Conductance.** The magnetic configuration of the A-type layered antiferromagnetic insulator—specifically, the angle  $\theta$  between the magnetic moments in neighboring layers—can impact the spin-filtering effect when constructing an MTJ device that uses this antiferromagnet as the tunnel barrier (*SI Appendix, Text 2*). Consequently, the tunneling magneto-conductance can serve as a measurable parameter for experimentally assessing the magnetic state. In the following sections, we will calculate the tunneling conductance using micromagnetic energy simulations at selected in-plane magnetic field strengths, as shown in Fig. 2, for both bilayer and trilayer systems, and we will aim to compare these findings with the experimental results.

In the case of a tunnel junction with a bilayer barrier (Fig. 2*A–F*), the tunneling current (normalized to its respective maximum) displays isotropic behavior at zero-field and over the



**Fig. 1.** Micromagnetic energy of an A-type antiferromagnet and schematic of the magnetic state transition. (A–F) Contour plots of micromagnetic energy at selected in-plane magnetic field's orientations of bilayer antiferromagnets. Corresponding  $\delta$  value (in degrees) is displayed above each plot. (D–F) are zoom-in plots of the micromagnetic energy's minimum located in lower-right of (A–C). (G) Cosine of angle ( $\theta$ ) between magnetic moments in adjacent layers as a function of the in-plane field direction in a bilayer antiferromagnet. (H–M) Contour plots of micromagnetic energy at selected in-plane magnetic field's orientations of trilayer antiferromagnets. (N) Cosine of angle ( $\theta$ ) between magnetic moments in adjacent layers as a function of the in-plane field direction in a trilayer antiferromagnet. Insets in (A) and (H–M) are simplified schematics showing energy models, with balls depicting stable states. In (A) and (H), orange solid arrows point from the simplified model to the minimum points of the energy contours. In (G and N), black curved arrows indicate the corresponding  $\delta$  angle range for contour plots in (A–F and H–M), respectively, with the spin configurations (represented by blue arrow for 1st [and 3rd in (N)] layer and green arrow for 2nd layer) and external field directions (indicated by dark red arrows) illustrated around the plot. The tilts of magnetic moments are exaggerated for clarity. Parameters used in (A–G):  $\mu_0 H_E = 0.86$  T,  $\mu_0 H = 0.6$  T,  $\mu_0 H_A = 1$  mT and (H–N):  $\mu_0 H_E = 0.96$  T,  $\mu_0 H = 0.5$  T,  $\mu_0 H_A = 1$  mT.

saturation field, as a result of the complete alignment of the magnetic moments in each layer with easy axis and the applied field, respectively. When a moderate external field is applied, spin–flop transition happens and the curves exhibit spindle shapes, with long-axis oriented in the direction of the assumed easy axis. This phenomenon arises because the anisotropy behaves like an additional magnetic field superimposed on the external field. As a result, the magnetic moments in each layer tend to align more with the field direction when it is aligned with the easy axis, leading to a decreased spin-filtering effect and increased tunneling conductance. (See *SI Appendix, Fig. S12* for schematics of the spin configurations in bilayer system.)

On the other hand, the tunneling current in a trilayer barrier system (Fig. 2 G–L) displays unique behaviors under varying external fields. When the magnetic field is below the spin–flop threshold ( $H < 0.5H_E$ ), the trilayer antiferromagnetic configuration shows minimal response to uniaxial anisotropy, exhibiting only slight modulation as the field direction changes. This is due to the fact that within this range, the magnetic moments in each layer align closely with the external field (either parallel or antiparallel) and experience only minor deviation from the field direction under influence of anisotropy (Fig. 2H, also see *SI Appendix, Fig. S13, B and G*). As the magnetic field approaches the spin–flop threshold ( $0.5H_E - \Delta H_1 < H < 0.5H_E + \Delta H_2$  where  $\Delta H_1$  and  $\Delta H_2$  are small quantities denoting the threshold range, see *SI Appendix, Text 4* for details), the micromagnetic energy undergoes a transition from bistable state to a unistable state (Fig. 1 H–N), characterized by

a shift of the system state in  $\phi - \theta$  phase space from one minimum to another. The change in  $\theta$  following the state transition, which determines the spin-filtering effect, results in a sudden alternation of the tunneling conductance as shown in Fig. 2I (also see *SI Appendix, Fig. S13 C and H*). Upon further increase of the magnetic field, both stable states of the micromagnetic energy persist throughout the entire circle of the field rotation, leading to a smooth variation of the magnetoresistance curve with a spindle shape (Fig. 2 J–K), similar to even-layer systems. A unique feature is that the long-axis of the spindle is not fixed, initially being nearly perpendicular to the easy axis at low fields and gradually rotating toward the direction of the easy axis as  $H$  increases. The variation in TMR response observed between odd- and even-layer antiferromagnetic barrier MTJs, regarding changes in the spindle-shaped current pattern direction under moderate magnetic fields, can be explained by differences in magnetic configurations (*SI Appendix, Text 7*). As a supplement to the above discussions, more detailed presentations with spin configurations under varying external field orientations are shown in *SI Appendix, Text 9 and Figs. S12 and S13*.

**Anisotropic Spin-Filtering in a  $\text{CrCl}_3$  MTJ.** To validate the above analysis through experimentation, we construct MTJ devices employing few layer  $\text{CrCl}_3$  as the barrier and assess the layer-dependent tunneling conductance while varying the rotating magnetic field.  $\text{CrCl}_3$  exhibits a layered A-type antiferromagnetic configuration with the magnetic moments aligned parallel within the ab-plane and antiparallel layer by layer in c direction (31,



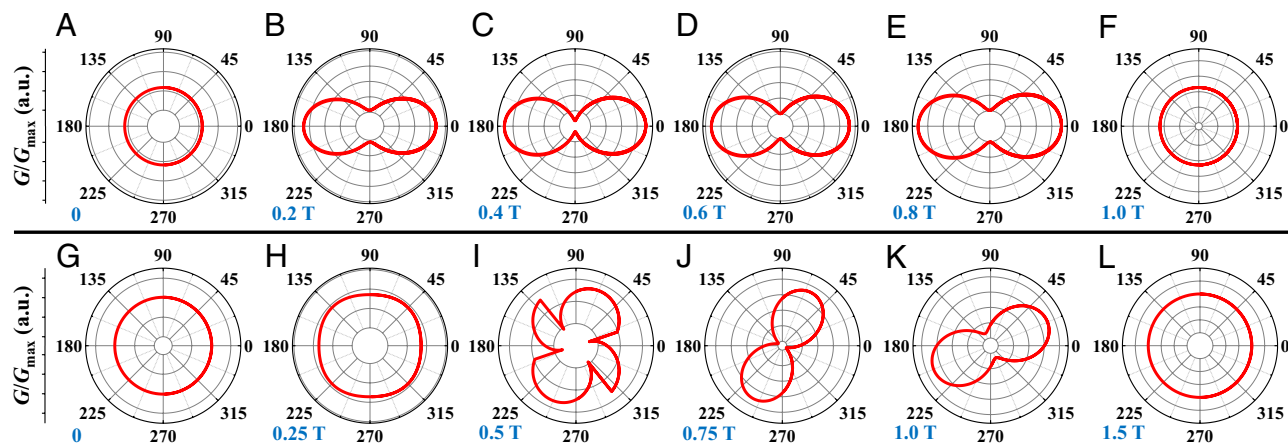


**Fig. 2.** Simulation results of normalized tunneling magneto-conductance. (A–L) Normalized tunneling magneto-conductance as a function of the in-plane field direction for MTJ with a bilayer (A–F) or trilayer (G–L) A-type antiferromagnetic barrier. The orderly arranged magnetic field  $\mu_0 H$  is 0 (A), 0.2 T (B), 0.4 T (C), 0.6 T (D), 0.8 T (E), 1 T (F) for bilayer device and 0 T (G), 0.25 T (H), 0.5 T (I), 0.75 T (J), 1 T (K), 1.5 T (L) for trilayer device, respectively. The easy axis is set to be horizontal.

35–40). Monolayer  $\text{CrCl}_3$  has been identified as an ideal easy-plane 2D magnet conforming to 2D-XY model, through a delicate X-ray magnetic circular dichroism (XMCD) experiment on high-quality epitaxial  $\text{CrCl}_3$  single layer (7). For multilayer  $\text{CrCl}_3$ , various studies indicate the presence of a subtle in-plane anisotropy (17, 30–32), with lattice distortions (17) or negative thermal expansion (32) playing a role in its manifestation. Consequently, the MTJ based on multilayer  $\text{CrCl}_3$  tunnel barrier represents an excellent system for investigating the ultraweak magnetic anisotropy. In this article, we mainly examine the layer-dependent behavior of tri- and tetralayer  $\text{CrCl}_3$  MTJ devices.

The illustration of a typical device with trilayer  $\text{CrCl}_3$  barrier (thickness  $\approx 1.74 \text{ nm}$  determined by atomic force microscopy in Fig. 3C bottom inset) is depicted in Fig. 3A. The optical micrograph of the same device is presented in Fig. 3C top inset. The  $\text{CrCl}_3$  crystal is sandwiched between top and bottom few-layer graphene electrodes to form an MTJ, further encapsulated by two thin hexagonal boron nitride (hBN) flakes to prevent degradation. The junction area measures less than  $1 \mu\text{m}^2$  to mitigate potential lateral magnetic domain influences (*Materials and Methods* for fabrication details). We first examine the tunneling current under zero-field cooling with a dc bias voltage of  $V_t = 1 \text{ V}$  (Fig. 3B). The resulting curve exhibits a kink at

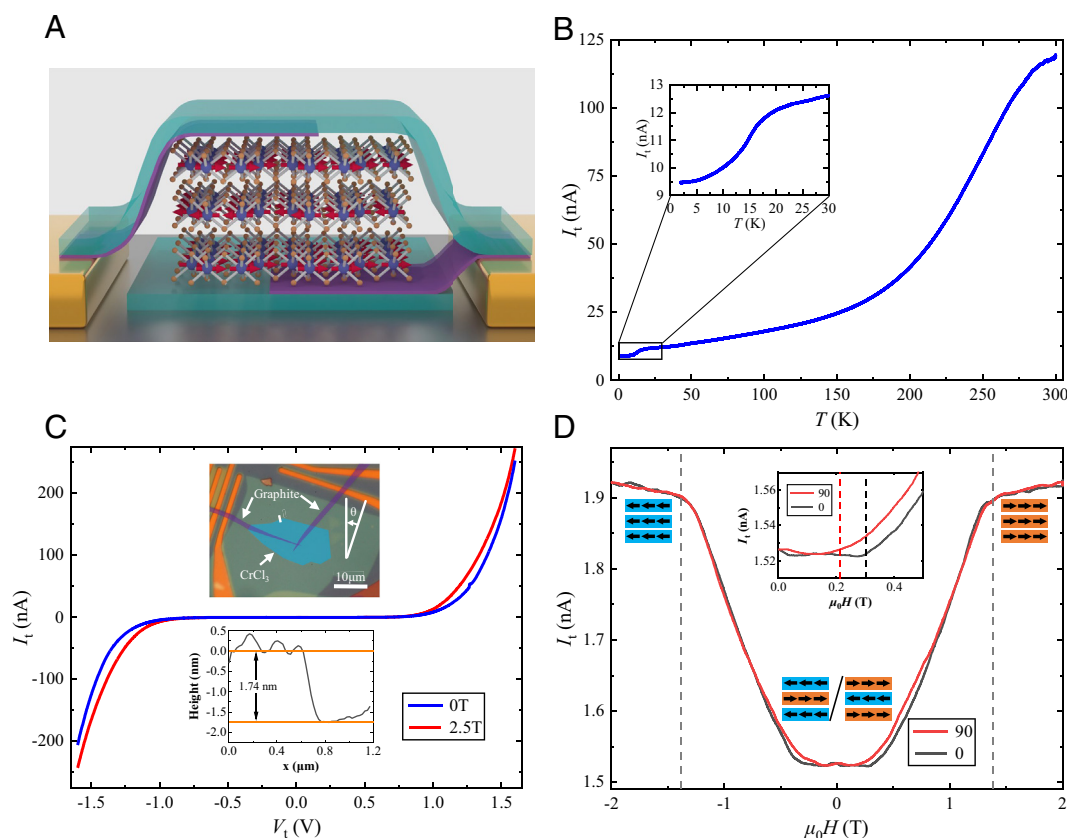


**Fig. 3.** Spin-filtering in a trilayer  $\text{CrCl}_3$  magnetic tunnel junction (MTJ). (A) Schematic of the device. Trilayer  $\text{CrCl}_3$  comes into contact with few-layer graphene (shown in purple), and the sandwiched structure is encapsulated by hBN (shown in cyan). Red arrows indicate the orientation of the magnetic moments in each  $\text{CrCl}_3$  layer. (B) Tunneling current as a function of the temperature at zero magnetic field and with an applied dc bias voltage of  $V_t = 1 \text{ V}$ . Inset: zoom-in plot in the temperature range between 2 and 30 K. (C) Tunneling current as a function of the bias voltage at zero field (blue line) and  $\mu_0 H = 2.5 \text{ T}$  (red line), respectively. Top inset: optical micrograph of Device 3L-1 with false color. Polar coordinate system used for subsequent measurements is indicated, which has already been adjusted to make the polar axis ( $0^\circ$ ) along with the presumptive easy axis. Bottom inset: AFM characterization along the short white line in the optical image. (D) Tunneling current as a function of the in-plane magnetic field at selected polar angles, under a dc bias voltage of  $V_t = 800 \text{ mV}$ . Antiferromagnetic-ferromagnetic transition field is marked with gray dashed lines. Inset: zoom-in plot of the low-field tunneling response, spin-flop fields are marked with dashed lines in black ( $0^\circ$ ) and red ( $90^\circ$ ). Magnetic configurations under different external fields are indicated. All electrical measurements in (C and D) are carried out at  $T = 2 \text{ K}$ .

ferromagnetic transition field is marked with gray dashed lines. Inset: zoom-in plot of the low-field tunneling response, spin-flop fields are marked with dashed lines in black ( $0^\circ$ ) and red ( $90^\circ$ ). Magnetic configurations under different external fields are indicated. All electrical measurements in (C and D) are carried out at  $T = 2 \text{ K}$ .

~15 K, which is enlarged in the inset, and is attributed to increased spin-filtering effect due to the paramagnetic-to-antiferromagnetic transition. Subsequently, the tunneling current  $I_t$  as a function of dc bias  $V_t$  at a base temperature of  $T = 2$  K is shown in Fig. 3C, demonstrating typical tunnel junction behavior. Introducing an in-plane magnetic field of  $\mu_0 H = 2.5$  T (red line) leads to an increase in tunneling conductance compared to the zero-field result (blue line), indicating the anticipated negative magneto-resistance for a layered antiferromagnetic barrier. We then fix the bias voltage of  $V_t = 800$  mV and measure the tunneling current as a function of the in-plane magnetic field. In Fig. 3D, we present curves under two distinct field directions, differing by  $90^\circ$ , which exhibit noticeable differences indicative of spin-flop behavior consistent with expectations of a uniaxial anisotropy model: When the magnetic field is aligned with the easy axis, anisotropy increases the potential barrier that needs to be overcome for spin-flop to happen, leading to higher spin-flop field, whereas when the external field is perpendicular to the easy axis, there is no such effect. As a result, when rotating the external field in-plane, a periodic fluctuation of the spin-flop field should be observed (SI Appendix, Text 6 and Fig. S7). The exchange field in this device, estimated to be approximately 0.92 T, can be derived from the magneto-conductance data, specifically from the derivative of conductance with respect to magnetic field, as illustrated in SI Appendix, Fig. S9. The measured spin-flop field ( $\mu_0 H_{sf} \approx 0.31$  T) being smaller than the analytically predicted  $0.5 H_E$  may be attributed to minor degradation of the device during fabrication process.

#### Anisotropic Tunneling Current with In-Plane Field Rotation.

We next conduct dc tunneling current measurements while continuously rotating the in-plane field to further investigate the magnetic anisotropy of the device. Fig. 4A and F show that the tunneling current displays isotropic behavior at zero-field and over the saturation field. When a finite magnetic field below  $\mu_0 H_{sf}$  is applied, the current is slightly influenced by the direction of the magnetic field (Fig. 4B). As the field approaches the spin-flop point ( $\mu_0 H = \frac{1}{2} \mu_0 H_E = 0.46$  T, SI Appendix, Text 1), multiple abrupt changes in the tunneling current are observed (Fig. 4C),

consistent with the simulation result (Fig. 2I), which is attributed to the magnetic state transition. As the magnetic field increases further, no state transitions occur and the direction of magnetic moments of each layer only oscillates around a small angle range (refer to Fig. 2J and K), resulting in a spindle-shaped current curve, with its long-axis rotating toward the easy axis as the external field increases (Fig. 4D and E). Through comparison of experiments and simulations, a range estimation of the uniaxial anisotropy field of the trilayer  $\text{CrCl}_3$  sample can be given as 2.4 to 8.6 mT (SI Appendix, Text 8 and Figs. S10 and S11). This range is higher than that estimated in bulk material, potentially due to different crystal phases or lattice distortion caused by strain induced during the fabrication process (7, 41). For results of layer-dependent tunneling current of other tri- and tetralayer devices, SI Appendix, Text 5 and Fig. S4.

The investigation of the state transition near the spin-flop point is extended to different temperatures. In Fig. 5A, the tunneling current demonstrates four times of abrupt changes when a rotating in-plane magnetic field of  $\mu_0 H = 0.45$  T is applied at  $T = 2$  K. With increasing temperature, the relative amplitude of these current jumps gradually diminishes (Fig. 5B and C). At  $T = 20$  K, which is above the Néel temperature (~17 K) (31), the tunneling current becomes nearly isotropic (Fig. 5D). In addition to the aforementioned findings, we have observed that as temperature increases, the positions of jumps gradually shift away from angles typical at low-temperatures, aligning more with directions parallel or perpendicular to the assumed easy axis (Fig. 5E). This behavior has been noted in simulations when reducing the anisotropy term while keeping other parameters constant, suggesting a weakening of both anisotropy and magnetization as temperature rises (42). Consequently, as temperature moves away from absolute zero, thermal disturbances increase and magnetization declines, leading to a gradual reduction in the influence of anisotropy. Ultimately, above the material's magnetic ordering temperature, thermal effects completely obscure these jumps.

To conclude, we have presented a viable approach to detect magnetic anisotropy at the scale of approximately 1 mT in A-type layered antiferromagnetic/ferrimagnetic insulators. By solving the micro-magnetic energy function, we simulate and predict the tunneling

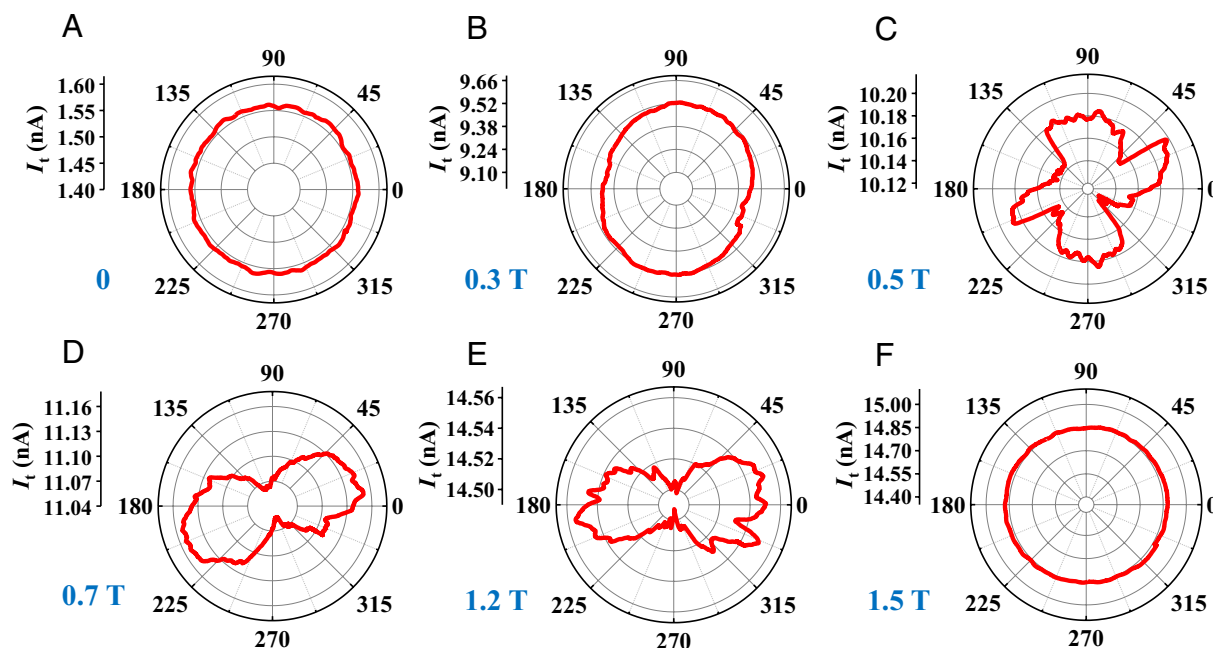


**Fig. 4.** Anisotropic tunneling current with continuous in-plane magnetic field rotation. (A–F) Tunneling current as a function of the polar angle of the in-plane magnetic field. The magnitude of the field is 0 T (A), 0.3 T (B), 0.5 T (C), 0.7 T (D), 1.2 T (E), 1.5 T (F). The field is rotated counterclockwise from 0 to  $360^\circ$  with a rotation speed of  $3^\circ$  per second. All measurements in (A–F) are carried out at the temperature  $T = 2$  K. The dc bias voltage is  $V_t = 800$  mV for (A) and  $V_t = 1.0$  V for (B–F).

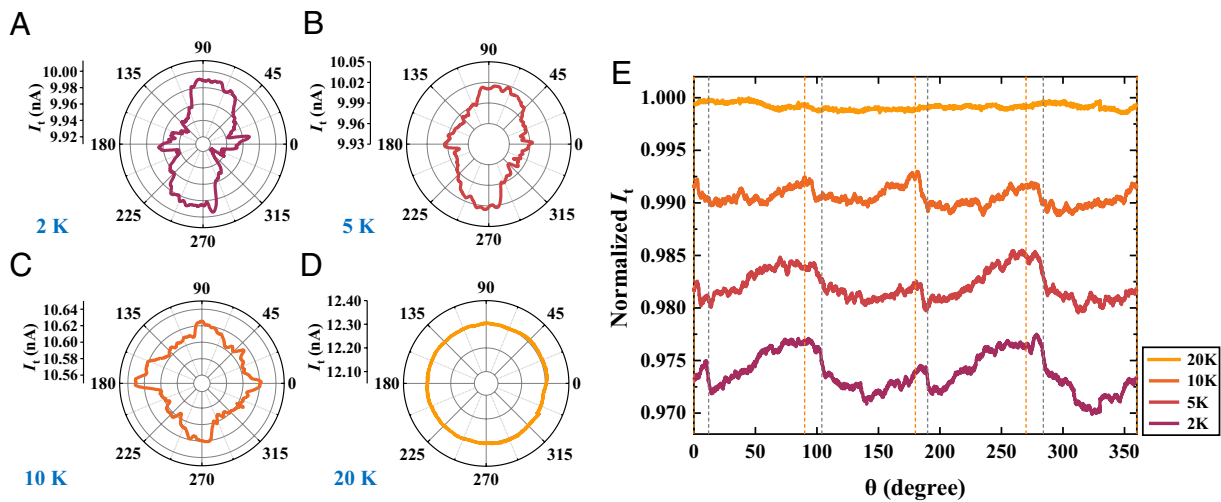


**Fig. 5.** Temperature-dependent tunneling current near the spin-flop point. (A–D) Tunneling current as a function of the polar angle of the in-plane magnetic field at  $T = 2$  K (A), 5 K (B), 10 K (C), and 20 K (D), respectively. The dc bias voltage is  $V_t = 1$  V and the magnitude of the field is  $\mu_0 H = 0.45$  T. (E) Summary of (A–D) in Cartesian system. In (E), all curves are normalized to their own maximum. Vertical offset between curves is used for clarity. Positions of the abrupt current changes at  $T = 2$  K and angles parallel or perpendicular to the easy axis are indicated with gray and orange dashed lines, respectively.

current curve under continuous rotation of in-plane magnetic field in an MTJ device using such a few-layer antiferromagnet/ferromagnet as the tunnel barrier. Experiments conducted on the in-plane antiferromagnetic insulator  $\text{CrCl}_3$  closely align with the simulation results, confirming the presence of a weak uniaxial magnetic anisotropy and validating the efficacy of our method. This method, serving as an effective strategy for probing magnetic anisotropy, holds promise for paving the way toward future spintronic applications and fundamental scientific exploration of van der Waals magnetic systems.

## Materials and Methods

**Device Fabrication.** Standard e-beam lithography procedures were employed to deposit prepatterned Cr (5 nm)/Au (30 nm) electrodes on a 285 nm  $\text{SiO}_2/\text{Si}$  substrate. Bulk  $\text{CrCl}_3$  crystals were acquired through chemical vapor transport (CVT). Few-layer  $\text{CrCl}_3$  nanoflakes were exfoliated onto 285 nm  $\text{SiO}_2/\text{Si}$  substrate from bulk crystals in a nitrogen-filled glove box, ensuring that the oxygen and water levels were kept below 0.1 ppm. Nanoflakes of suitable thickness were identified by optical contrast under a microscope. The MTJs were assembled by a standard dry transfer technique using poly (bisphenol A carbonate) (PC)/polydimethylsiloxane (PDMS) stamps, similar to methods reported in Ref. 43. The vertical structures predesigned of hBN/graphite/ $\text{CrCl}_3$ /graphite/hBN were sequentially picked up by stamp and finally transferred onto target substrate with the top and bottom graphite flakes contacted to the prepatterned electrodes by melting and solidifying PC thin film. The entire structure was either picked up at once, or only the top four layers were picked up and transferred onto a bottom hBN that had been previously positioned on the substrate. After the dry transfer process, the device (covered by a PC film) was removed from the glove box, and the PC film was dissolved in chloroform. Atomic force microscopy measurements were carried out after the complete fabrication

of the device to determine the thickness of the  $\text{CrCl}_3$  flakes. *SI Appendix, Table S1* summarizes the thickness of the  $\text{CrCl}_3$  in various devices investigated in our study.

**Electrical Measurements.** All electrical measurements were conducted in a Physical Property Measurement System (PPMS) with an Evercool cryostat (Quantum Design, Inc.) capable of applying magnetic field up to 9 T at a base temperature of  $T = 2$  K. The MTJ devices were mounted on a vertical rotation probe (Multifield Tech.), which allows rotation of magnetic field within the sample plane. Dc bias voltage was applied to the top graphite contact and the current from the bottom graphite contact was measured using a current preamplifier (DL Instruments, Model 1211) and a DAQ (National Instruments, USB-6212).

**Data, Materials, and Software Availability.** All study data are included in the article and/or *SI Appendix*.

**ACKNOWLEDGMENTS.** Shanghai Pilot Program for Basic Research–Shanghai Jiao Tong University 21TQ1400206 (X.C.), National Key Research and Development Program 2020YFA0309200 (X.C.), National Natural Science Foundation of China 62475149, 92064013, 11904226 (X.C.), Sichuan Science and Technology Program 2024YFH20264 (F.L.), National Key Research and Development Program 2021YFE0194200 (F.L.), National Natural Science Foundation of China 12161141015, 62074025 (F.L.).

Author affiliations: <sup>a</sup>National Key Laboratory of Advanced Micro and Nano Manufacture Technology, Shanghai Jiao Tong University, Shanghai 200240, China; <sup>b</sup>Department of Micro/Nano Electronics, School of Electronic Information and Electrical Engineering, Shanghai Jiao Tong University, Shanghai 200240, China; <sup>c</sup>School of Optoelectronic Science and Engineering, University of Electronic Science and Technology of China, Chengdu 611731, China; <sup>d</sup>National Institute for Materials Science, Tsukuba 305-0044, Japan; <sup>e</sup>Yangtze Delta Region Institute (Huzhou), University of Electronic Science and Technology of China, Huzhou 313001, China; and <sup>f</sup>State Key Laboratory of Electronic Thin Films and Integrated Devices, University of Electronic Science and Technology of China, Chengdu 611731, China

1. J. L. Lado, J. Fernández-Rossier, On the origin of magnetic anisotropy in two dimensional  $\text{CrI}_3$ . *2D Mater.* **4**, 035002 (2017).
2. J. Liu, M. Shi, J. Lu, M. P. Anantram, Analysis of electrical-field-dependent Dzyaloshinskii–Moriya interaction and magnetocrystalline anisotropy in a two-dimensional ferromagnetic monolayer. *Phys. Rev. B* **97**, 054416 (2018).
3. D. R. Klein *et al.*, Enhancement of interlayer exchange in an ultrathin two-dimensional magnet. *Nat. Phys.* **15**, 1255–1260 (2019).
4. R. Zhu *et al.*, Exchange bias in van der Waals  $\text{CrCl}_3/\text{Fe}_3\text{GeTe}_2$  heterostructures. *Nano Lett.* **20**, 5030–5035 (2020).
5. B. Huang *et al.*, Layer-dependent ferromagnetism in a van der Waals crystal down to the monolayer limit. *Nature* **546**, 270–273 (2017).
6. Z. Fei *et al.*, Two-dimensional itinerant ferromagnetism in atomically thin  $\text{Fe}_3\text{GeTe}_2$ . *Nat. Mater.* **17**, 778–782 (2018).
7. A. Bedoya-Pinto *et al.*, Intrinsic 2D-XY ferromagnetism in a van der Waals monolayer. *Science* **374**, 616–620 (2021).
8. T. Song *et al.*, Giant tunneling magnetoresistance in spin-filter van der Waals heterostructures. *Science* **360**, 1214–1218 (2018).
9. X. Wang *et al.*, Current-driven magnetization switching in a van der Waals ferromagnet  $\text{Fe}_3\text{GeTe}_2$ . *Sci. Adv.* **5**, eaaw8904 (2019).
10. I. Shin *et al.*, Spin-orbit torque switching in an all-van der Waals heterostructure. *Adv. Mater.* **34**, 2101730 (2022).
11. P. Wadley *et al.*, Electrical switching of an antiferromagnet. *Science* **351**, 587–590 (2016).
12. P. E. Roy, R. M. Otxoa, J. Wunderlich, Robust picosecond writing of a layered antiferromagnet by staggered spin-orbit fields. *Phys. Rev. B* **94**, 014439 (2016).
13. X. F. Zhou *et al.*, Strong orientation-dependent spin-orbit torque in thin films of the antiferromagnet  $\text{Mn}_2\text{Au}$ . *Phys. Rev. Applied* **9**, 054028 (2018).

14. W. Yu *et al.*, Chemically exfoliated VSe<sub>2</sub> monolayers with room-temperature ferromagnetism. *Adv. Mater.* **31**, 1903779 (2019).
15. T. Zhu *et al.*, Synthesis, magnetic properties, and electronic structure of magnetic topological insulator MnBi<sub>2</sub>Se<sub>4</sub>. *Nano Lett.* **21**, 5083–5090 (2021).
16. L. Alahmed *et al.*, Magnetism and spin dynamics in room-temperature van der Waals magnet Fe<sub>3</sub>GeTe<sub>2</sub>. *2D Mater.* **8**, 045030 (2021).
17. A. Narath, Low-temperature sublattice magnetization of antiferromagnetic CrCl<sub>3</sub>. *Phys. Rev.* **131**, 1929–1942 (1963).
18. C. Tang *et al.*, Spin dynamics in van der Waals magnetic systems. *Phys. Rep.* **1032**, 1–36 (2023).
19. Y. Deng *et al.*, Gate-tunable room-temperature ferromagnetism in two-dimensional Fe<sub>3</sub>GeTe<sub>2</sub>. *Nature* **563**, 94–99 (2018).
20. C. Gong *et al.*, Discovery of intrinsic ferromagnetism in two-dimensional van der Waals crystals. *Nature* **546**, 265–269 (2017).
21. T. Song *et al.*, Direct visualization of magnetic domains and moiré magnetism in twisted 2D magnets. *Science* **374**, 1140–1144 (2021).
22. G. Kim, J. Yun, Y. Lee, J. Kim, Construction of a vector-field cryogenic magnetic force Microscope. *Rev. Sci. Instrum.* **93**, 063701 (2022).
23. M. Lohmann *et al.*, Probing magnetism in insulating Cr<sub>2</sub>Ge<sub>2</sub>Te<sub>6</sub> by induced anomalous hall effect in Pt. *Nano Lett.* **19**, 2397–2403 (2019).
24. B. Niu *et al.*, Coexistence of magnetic orders in two-dimensional magnet CrI<sub>3</sub>. *Nano Lett.* **20**, 553–558 (2020).
25. Y. Zur *et al.*, Magnetic imaging and domain nucleation in CrSBr Down to the 2D limit. *Adv. Mater.* **35**, 2307195 (2023).
26. A. Noah *et al.*, Interior and edge magnetization in thin exfoliated CrGeTe<sub>3</sub> films. *Nano Lett.* **22**, 3165–3172 (2022).
27. W. Chen *et al.*, Direct observation of van der Waals stacking-dependent interlayer magnetism. *Science* **366**, 983–987 (2019).
28. L. Thiel *et al.*, Probing magnetism in 2D materials at the nanoscale with single-spin microscopy. *Science* **364**, 973–976 (2019).
29. X. Fan, D. Xue, C. Jiang, Y. Gong, J. Li, An approach for researching uniaxial anisotropy magnet: Rotational magnetization. *J. Appl. Phys.* **102**, 123901 (2007).
30. B. Kuhl, Magnetic ordering in CrCl<sub>3</sub> at the phase transition. *Phys. Status Solidi* **72**, 161–168 (1982).
31. M. A. McGuire *et al.*, Magnetic behavior and spin-lattice coupling in cleavable van der Waals layered CrCl<sub>3</sub> crystals. *Phys. Rev. Mater.* **1**, 014001 (2017).
32. T. P. Thomas *et al.*, Acoustically driven magnon-phonon coupling in a layered antiferromagnet. *Phys. Rev. Lett.* **131**, 196701 (2023).
33. Z. Wang *et al.*, Determining the phase diagram of atomically thin layered antiferromagnet CrCl<sub>3</sub>. *Nature Nanotechnol.* **14**, 1116–1122 (2019).
34. U. K. Rößler, A. N. Bogdanov, Magnetic phases and reorientation transitions in antiferromagnetically coupled multilayers. *Phys. Rev. B* **69**, 184420 (2004).
35. H. H. Kim *et al.*, Evolution of interlayer and intralayer magnetism in three atomically thin chromium trihalides. *Proc. Natl. Acad. Sci. U. S. A.* **116**, 11131–11136 (2019).
36. X. Cai *et al.*, Atomically thin CrCl<sub>3</sub>: An in-plane layered antiferromagnetic insulator. *Nano Lett.* **19**, 3993–3998 (2019).
37. H. H. Kim *et al.*, Tailored tunnel magnetoresistance response in three ultrathin chromium trihalides. *Nano Lett.* **19**, 5739–5745 (2019).
38. L. Liu *et al.*, Accelerated degradation of CrCl<sub>3</sub> nanoflakes induced by metal electrodes: Implications for remediation in nanodevice fabrication. *ACS Appl. Nano Mater.* **2**, 1597–1603 (2019).
39. S. Kazim *et al.*, Mechanical exfoliation and layer number identification of single crystal monoclinic CrCl<sub>3</sub>. *Nanotechnology* **31**, 395706 (2020).
40. Y. Wu *et al.*, Magnetic exchange field modulation of quantum hall ferromagnetism in 2D van der Waals CrCl<sub>3</sub>/graphene heterostructures. *ACS Appl. Mater. Interfaces* **13**, 10656–10663 (2021).
41. J. O'Donnell, M. S. Rzchowsky, J. N. Eckstein, I. Bozovic, Magnetoelastic coupling and magnetic anisotropy in La<sub>0.67</sub>Ca<sub>0.33</sub>MnO<sub>3</sub> films. *Appl. Phys. Lett.* **72**, 1775–1777 (1998).
42. H. B. Callen, E. Callen, The present status of the temperature dependence of magnetocrystalline anisotropy, and the l(l+1)/2 power law. *J. Phys. Chem. Solids* **27**, 1271–1285 (1966).
43. P. J. Zomer, M. H. D. Guimarães, J. C. Brant, N. Tombros, B. J. van Wees, Fast pick up technique for high quality heterostructures of bilayer graphene and hexagonal boron nitride. *Appl. Phys. Lett.* **105**, 013101 (2014).